https://doi.org/10.1016/j.jpowsour.2020.229337
This is the Pre-Published Version.

Boosted lithium storage cycling stability of TiP_2 by *in-situ* partial self-decomposition and nano-spatial confinement

Fengchen Zhou[a], Xu-Sheng Yang[c,d*], Jiangwen Liu[a], Jun Liu[a], Renzong Hu[a], Liuzhang Ouyang[a,b**], Min Zhu[a]

[a] School of Materials Science and Engineering, Guangdong Provincial Key Laboratory of Advanced Energy Storage Materials, South China University of Technology, Guangzhou, 510641, China. Email: meouyang@scut.edu.cn

[b] China-Australia Joint Laboratory for Energy & Environmental Materials, Key Laboratory of Fuel Cell Technology of Guangdong Province, Guangzhou, 510641, China

[c] Advanced Manufacturing Technology Research Centre, Department of Industrial and Systems Engineering, The Hong Kong Polytechnic University, Hung Hom, Kowloon, Hong Kong, China. Email: xsyang@polyu.edu.hk

[d] Hong Kong Polytechnic University Shenzhen Research Institute, Shenzhen 518057, China

[*]Corresponding authors.
[a**] E-mail: meouyang@scut.edu.cn, (L. Ouyang)
[c*] E-mail: xsyang@polyu.edu.hk, (X. Yang)

© 2020. This manuscript version is made available under the CC-BY-NC-ND 4.0 license http://creativecommons.org/licenses/by-nc-nd/4.0/

Abstract:

Titanium phosphide (TiP_2) is particularly interesting due to its ability to form the stable Li-Ti-P ternary phase. However, TiP_2 faces the limitations in cyclic stability due to the volume change occurred by the destruction/recovery of the long-range cubic order Li-Ti-P phase, and unable to deliver high capacity. In this work, we propose the in-situ formation of electrochemically inactive TiP and phosphorus via partial decomposition of TiP_2 by ball milling process, achieving a multi-phase TiP_2-TiP-P-C composite. On one hand, the decomposition-formed TiP effectively relieve the stress caused by the formation of Li_xTiP_4 and LiP_3. On the other hand, another decomposition-formed small-sized phosphorus significantly reduce its volume change during the lithiation/delithiation cycles for the overall capacity. Accordingly, the synthesized multi-phase TiP_2-TiP-P-C with the above cooperative effects delivers a high capacity of 836.3 mAh g^{-1} at 0.2 A g^{-1} as high-performance Lithium-ion battery anode. In addition, a notable capacity retention of 81.4 % is also achieved after 1000 cycles at 5 A g^{-1}. Furthermore, when paired with $LiFePO_4$ cathode in a full cell, the excellent specific capacity, cycling and rate performance can also be obtained. The rational design of TiP_2-TiP-P-C will be beneficial towards the future development of metal-phosphide-phosphorous composite as LIB anode.

Keywords: TiP_2, TiP, in-situ formation, phase boundary, lithium-ion battery

1. Introduction

With the rapid digitization in the society, energy storage devices with high electrochemical performance are greatly desired. Being the forerunner in energy storage technology, lithium-ion battery (LIB) is still revered as the key battery technology widely used in commercial applications. However, with the increasing fixation in achieving high-performance battery for these applications, the current LIB technology may deem to be inadequate to fully meet the demands. Since the performance of LIB is largely due to the electrode materials, there is a great urgency to develop alternative LIB anode material replacing the commercial graphite to achieve high performing LIB.

In recent years, metal phosphides have triggered significantly research interest as the potential LIB anode materials due to their relatively low intercalation potentials and high theoretical capacities.[1-11] In addition, these materials can be prepared via a simple and cost-effective mechanical ball milling synthesis route which can be easily scaled up.[12] Till now, the Li^+ storage mechanisms of metal phosphides can generally be classified into two categories, *i.e.* conversion mechanism [1-7, 13] and intercalation mechanism.[8-11] It is well-known that conversion mechanism can lead to higher capacities as compared to intercalation mechanism. However, the larger volume change induced by conversion mechanism can inevitably lead to the pulverization of the material during cycling. In this regard, intercalation-type metal phosphides are able to exhibit low volume expansion, potentially leading to a more durable cyclic operation as compared to conversion/alloying type materials.[8-11] For example, Titanium based intercalation metal phosphides are highly attractive due to the formation of a stable Li-Ti-P ternary phase during discharge/charge process, which allows the reversible intercalation/extraction of Li^+ into/out of the host matrix.[10] As such, TiP_2 has been reported as a potential LIB anode material with generally encouraging performances.[11, 14] However, due to the structural change arising from the repeated destruction/recovery of the long-range

cubic order in Li_xTiP_4, TiP_2 typically suffers from capacity degradation.[11] Furthermore, its achievable capacity is still inferior as compared to the conversion-based anode material which leads to the current urge to further increase its capacity via incorporation of a small amount of alloying/conversion-type materials. Leveraging the capacity contribution from phosphorous is an effective strategy due to its high theoretical capacity of 2560 mAh g^{-1}. This strategy is particularly suitable for TiP_2 since phosphorus is one of the precursors used in its synthesis.[14] Thus, by increasing the ratio of Ti powder to phosphorus from an ideal stoichiometry of 1: 2, excess phosphorus powder (beyond 1:2) can be used to prepare the TiP_2-P system. As such, the high content of excess coarse phosphorus powders can lead to high capacity, but at the expense of cyclic stability due to the well-known massive volume change experienced by phosphorus during cycling.

In order to increase the appeal of TiP_2 as LIB anode, this work proposes to partially decompose TiP_2 to form TiP and phosphorus, forming TiP_2-TiP-P-C composite. The rationale of this strategy is of two folds: (1) Formation of electrochemically inactive TiP in the system can help to buffer the volume exchange as itself does not exhibit volume change during cycling.[10, 11, 15] (2) another decomposed phosphorus should be smaller in size as compared to the traditionally ball-milled phosphorus powder, which can address the volume change in P during cycling with the nano-sizing effect.[16, 17] Furthermore, the multi-phase structure (among TiP_2-TiP-P-C) can effectively accommodate the volume change due to the constraint from the increased interfaces.[18, 19] Hence, it is expected that the proposed multi-phase TiP_2-TiP-P-C composite can simultaneously derive its capacity from the alloying reaction of phosphorus and maintain a more robust cyclic stability due to these stabilization strategies.

Herein, a unique multi-phase TiP_2-TiP-P-C composite is successfully synthesized using a high energy ball milling process and investigated as a potential LIB anode in this work. Based on the electrochemical performance evaluation, a high capacity of 836.3 mAh g^{-1} is recorded

for the multi-phase TiP_2-TiP-P-C at a current density of 0.2 A g^{-1}. Even with 50 times increment in the current density (10 A g^{-1}), it is still able to achieve good rate capability of 525.9 mAh g^{-1}. More impressively, multi-phase TiP_2-TiP-P-C composite is able to demonstrate excellent cyclic stability of 89.1 % after cycling for 500 cycles at 2 A g^{-1}, which is, to the best of our knowledge, one of the best cyclic stability for the reported TiP_2 systems. The robustness of the cyclic stability for the multi-phase composite is further verified by a notable 81.4 % capacity retention after cycling for 1000 cycles at 5 A g^{-1}. Thus, this one-step strategy of partially decomposing TiP_2 into electrochemically inactive TiP and capacity contributing phosphorus via high energy ball-milling will be highly beneficial towards the future development of high-performance metal-phosphide-phosphorous composite LIB anode.

2. Experimental section

2.1 Materials synthesis

2.1.1 Chemicals

Ti (99.9% purity) and red phosphorus powders (98.5% purity) were purchased from Aladdin Co., Ltd. Expanded graphite (EG) was obtained by putting expandable graphite (99.9% purity, 100 mesh, Qingdao Xinghua Co., Ltd.) in a furnace at 950 °C for 120 seconds under an air atmosphere. D.I water was used for all experiments unless otherwise specified.

2.1.2 Synthesis of TiP_2-TiP-P-C

First, Ti and red phosphorus powders in the molar ratio of 1:2 were ball milled using a high-energy shaking ball mill (QM-3C) for a duration of 2 h to achieve TiP_2. Then, the as-synthesized TiP_2 and EG were mixed in the weight ratio of 7:3, to be ball milled for the fabrication of TiP_2-TiP-P-C by using shaking ball mill for a duration of 3 h. All ball milling processes were conducted under Argon protection gas with the weight ratio between ball and material of 50:1, and the milling speed of 1200 rpm min^{-1}.

2.1.3 Synthesis of TiP_2-C, TiP_2-TiP-C and TiP_2-P-C

In order to study the individual and cooperative electrochemical effects of two decomposed byproducts TiP and P, the other three counterparts, i.e., TiP_2-C, TiP_2-TiP-C and TiP_2-P-C, were also prepared (without the decomposition of TiP_2) for the comparison. The TiP was prepared using the same procedure as that for TiP_2 whereby a molar ratio of Ti to red phosphorus powder was changed to 1:1. The procedures of ball milling with planetary ball mill (QM-3A) (a duration of 20 h at 400 rpm min^{-1}) were employed to synthesize TiP_2-C, TiP_2-TiP-C and TiP_2-P-C. In addition, the contents of EG, TiP and P in these composites were also equivalent to that in TiP_2-TiP-P-C composite.

2.2 Materials characterization

X-ray diffractometer (Panalytical Empyrean) with Cu-Ka radiation and X-ray photoelectron spectrometer (Thermo Scientific ESCALAB 250) were used to record the X-ray diffraction patterns (XRD) and X-ray photoelectron spectra (XPS), respectively, for analyzing the phase constitutes of the samples. In addition, scanning electron microscope (SEM, Carl Zeiss Supra 40) and transmission electron microscope (TEM, JEOL JEM-2100) operating at 200 kV were used to observe the morphologies of the samples.

2.3 Electrochemical characterization

In a typical preparation of the working electrode, the active material (70 wt%) was mixed homogeneously with Super P (15 wt%) and carboxymethyl cellulose (CMC) (15 wt%) in deionized water. The prepared slurry was later pasted onto a copper foil for drying overnight at 100 °C under vacuum condition. The film was subsequently cut into a disk-like electrode with a diameter of 12 mm. The active material loading density was determined to be *ca.* 0.7-0.8 mg cm^{-2}. The test cells were then assembled with lithium foils as the counter electrode in an argon-filled glove box. 1 M $LiPF_6$ in EC/DEC/DMC (1:1:1 in vol.), with the addition of 10 wt% FEC, was used as the electrolyte. Galvanostatic cycling tests were conducted using a LAND CT2001A battery testing system between a potential window of 0.01-2.0 V (*vs.* Li^+/Li).

Cyclic voltammetry (CV) curves were obtained at various scan rates between a potential window of 0.01-2.0 V using a Gamry Interface 1000 electrochemical workstation. The cycled electrodes were disassembled and washed with DEC and dried for several days in the glovebox before the post-mortem characterization. In addition, full cells were assembled by pairing TiP_2-TiP-P-C electrode (as the anode) with commercial $LiFePO_4$ (LFP) electrode (as the cathode). And the N/P ratio of the full cell was designed to be about 1:1.5 with a slightly excess lithium content of positive to investigate the releasing capacity limitation of anode material. LFP electrode was prepared by mixing the active material (80 wt%) with Super P (10 wt%) and polyvinylidene fluoride (10 wt%) homogeneously. CV curves of the full cell, denoted as LFP||TiP_2-TiP-P-C, were measured between a voltage window of 1.0 and 3.5 V at a scan rate of 0.2 mV s^{-1}. Galvanostatic discharge/charge tests of LFP||TiP_2-TiP-P-C were conducted in a voltage window between 1.0-3.5 V. The mass of anode active material was used for the calculation of current densities and specific capacities reported in this work.

3. Results and discussion

Fig. 1a shows the schematic illustration of the synthesis process of TiP_2-TiP-P-C composite. *Via* a ball milling process, the TiP_2 can in-situ decompose into TiP and P to synthesize a multi-phase TiP_2-TiP-P-C composite. Fig. 1b first give the XRD patterns of synthesized TiP_2 and TiP_2-TiP-P-C, respectively, in which the diffraction peaks of the ball-milled TiP_2 sample with Ti and P powders in the molar ratio of 1:2 can be well-matched with the standard pattern of TiP_2 (JCPDS NO. 73-1835). This result indicates that such ball milling process in this work is able to successfully fabricate TiP_2. In addition, Fig. 1b also shows that the characteristic peaks of TiP_2 are still presented in the XRD pattern of TiP_2-TiP-P-C composite, which is synthesized by shaking ball milling the TiP_2 with EG. Interestingly, the additional peaks of TiP (JCPDS NO. 73-1821) can be identified in the XRD pattern of TiP_2-TiP-P-C composite. This result suggests that the TiP_2 phase is partially decomposed to TiP phase along with the concomitant

P during the shaking ball milling process of TiP_2 with EG, following the decomposition reaction as: $TiP_2 \rightarrow TiP + P$.[15] Rietveld refinement of the XRD spectrum is performed to quantitatively estimate the weight percentages of various components in the composites, as shown in Fig. 1c. It is turned out that the weight ratio of TiP_2:TiP is 79:21, and the overall weight ratio of TiP_2, TiP, P, and EG in TiP_2-TiP-P-C is approximately 51.1, 13.6, 5.3 and 30 respectively. Fig. S1a in supplementary information also gives the XRD pattern of TiP_2-C composite synthesized by a planetary ball milling of TiP_2 with EG, instead of shaking ball milling, which used as the control sample in this work. It indicates that the TiP_2 is able to maintain the original crystal structure without any sign of decomposition during the planetary ball milling process. Moreover, Fig. 1d and Fig. 1e show respectively the high-resolution XPS spectrum of C 1s and P 2p of TiP_2-TiP-P-C composite. It is noted that the five peaks which are located at 284.2 eV (C-P bond), 284.8 eV (sp^2 C-C bond), 285.6 eV (sp^3 C-C), 286.8 eV (C=O) and 289.2 eV (O-C=O), respectively, are deconvoluted from C 1s XRS spectrum, as shown in Fig. 1d.[20-22] While, Fig. 1e shows that four peaks can be deconvoluted from the P 2p XPS spectrum at 129.0eV, 129.7 eV, 130.3 eV and 133.5 eV, respectively, which can be correspondingly assigned to the Ti-P bond,[23] P-P bond with amorphous P,[24] P-C bond and P-O bond.[22, 25] Fig. 1f shows the high-resolution Ti 2p XPS spectrum of all three composites, *i.e.* TiP_2-TiP-P-C, TiP_2-C, and TiP-C. The Ti 2p XPS spectrum of TiP_2-TiP-P-C can be deconvoluted with two pairs of peaks that can be well matched to the superpositions of TiP_2-C and TiP-C. This indicates that TiP_2-TiP-P-C composite consists of both TiP_2 and TiP, which is consistent with the XRD result (Fig. 1b). Furthermore, by calculating the area of the two pairs of peaks of TiP_2 TiP, the molar ratio of TiP_2:TiP can be estimated as *ca.* 2.67, which agrees well with the Rietveld refinement result (Fig. 1c). Besides, the peak at 455.0 eV can be attributed to Ti-C bond.[25] It is worth noting that the existence of Ti-C bond can enhance the connection between TiP_x and C, thus further improving the electronic migration. The high-

resolution C 1s and P 2p XPS spectrum of TiP_2-C are similar to those of TiP_2-TiP-P-C composite, as indicated in Fig. S1.

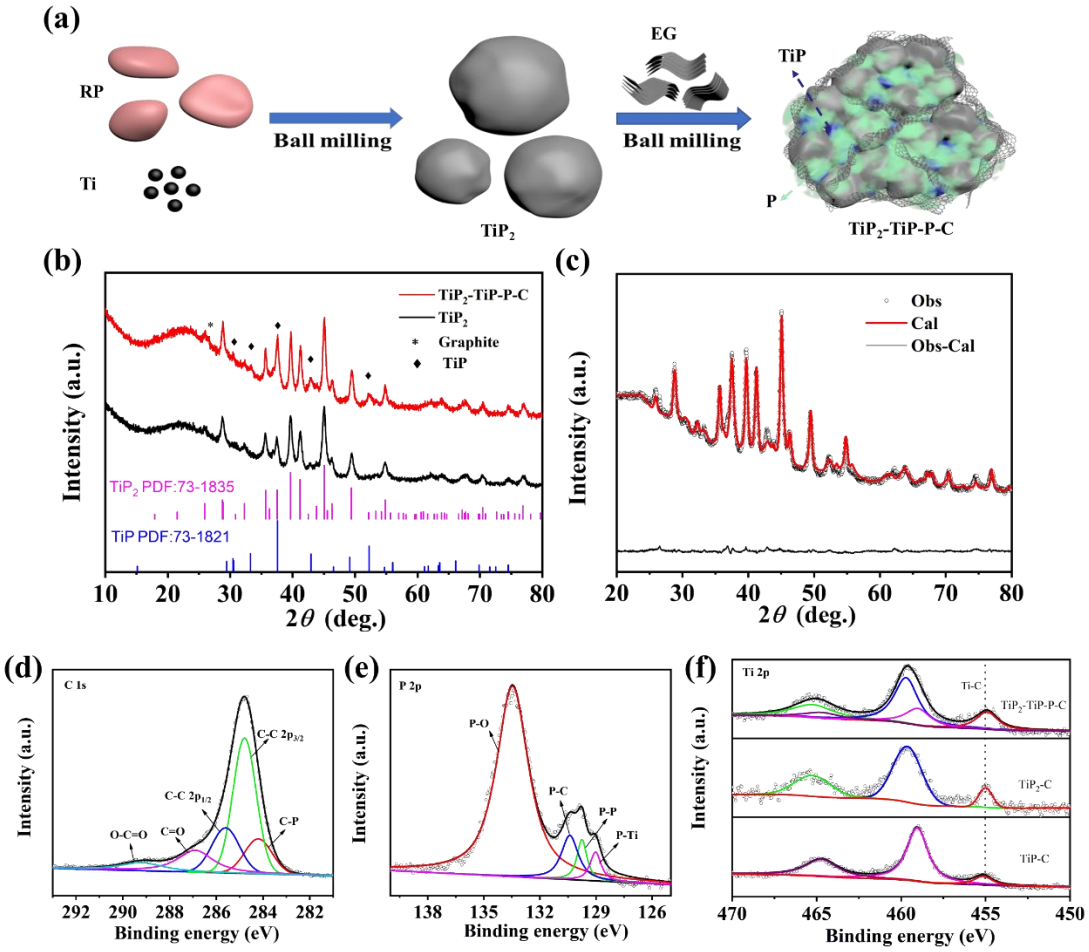

Fig. 1 (a) Schematic illustration of the fabrication of the BP-TiO2-C composite, (b) XRD patterns of TiP_2 and TiP_2-TiP-P-C, (c) Rietveld refined XRD pattern of TiP_2-TiP-P-C. High-resolution XPS spectra of (d) C 1s, (e) P 2p, and (f) Ti 2p of TiP_2-TiP-P-C compared with TiP_2-C and TiP-C.

SEM and TEM were performed to observe and investigate the morphology of TiP_2-TiP-P-C composite in Fig. 2. More specifically, Fig. 2a and 2b show respectively the SEM images of TiP_2 (insets in Fig. 2a are SEM images of the original commercial Ti and P powders) and TiP_2-TiP-P-C. It can be seen from Fig. 2a that the TiP_2 exhibits a micro-sized granular structure which is composed of a tremendous number of nano-sized primary particles. After ball milling with EG, the micro-sized TiP_2 granular particles are destroyed severely, as shown in Fig. 2b, to form the TiP_2-TiP-P-C composite with irregular nanoparticles. The detailed morphology of

TiP_2-TiP-P-C composite is further investigated by the TEM observations. Fig. 2c shows that TiP_2-TiP-P-C nanocomposite consists of a mixture of nanocrystalline TiP_2 and TiP phases, as the typical lattice planar spacing identified from the selected area electron diffraction (SAED) pattern in Fig. 2d. Moreover, the HRTEM images in Fig. 2e and Fig. 2f directly measure the lattice planar spacing of the (302) and (111) for TiP_2, and (104) and $(10\bar{3})$ for TiP, which are well match the referenced data of these two crystals. Noticeably, TiP nanoparticle tends to adhere the surface of TiP_2 nanoparticle, suggesting the in-situ formation of TiP via the decomposition of TiP_2. In addition, these two nanoparticles are surrounded by the amorphous carbon. The multi-phase TiP_2-TiP-P-C nanocomposite can create a large number of interfaces, which can accelerate the migration of lithium-ion and enhance the storage capacity of more lithium-ion. For comparison, the SEM images of TiP_2 and TiP_2-C, and the HRTEM image of TiP_2-C are shown in Fig. S2-S3, respectively, where the TiP_2 is also surrounded by the amorphous carbon.

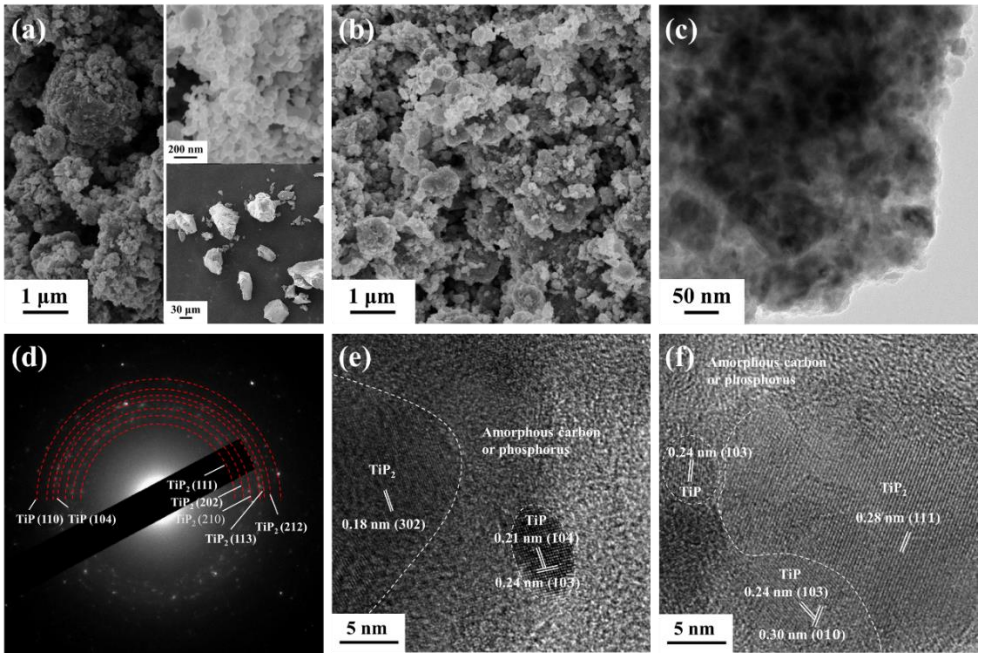

Fig. 2 SEM images of (a) the TiP_2 (the insets are SEM images of commercial Ti (top) and P (bottom) powders) and (b) TiP_2-TiP-P-C. (c) TEM image, (d) SAED, and (e, f) high-resolution TEM images of TiP_2-TiP-P-C.

Electrochemical performance of TiP_2-TiP-P-C and TiP_2-C electrodes are investigated in a potential window of 0.01-2.0 V (*vs.* Li^+/Li). Galvanostatic discharge/charge profiles of TiP_2-TiP-P-C electrode with various cycles at a current density of 500 mA g^{-1} are shown in Fig. 3a, where the initial discharge and charge capacities of TiP_2-TiP-P-C are 1071.6 and 868 mAh g^{-1}, respectively, with a high coulombic efficiency of 81.01%. In contrast, Fig. 3b indicates that the reversible discharge capacity of the TiP_2-C electrode is merely 735.8 mAh g^{-1}, with a lower initial coulombic efficiency of 70.15%. Cyclic voltammetry for TiP_2-TiP-P-C electrode was conducted at a scan rate of 0.1 mV s^{-1} between a potential window of 0.01-2.0 V (*vs.* Li^+/Li). Based on the CV profile of TiP_2-TiP-P-C electrode, as shown in Fig. 3c, the peak located at *ca.* 1.2 V can be identified during the initial cathodic scan, corresponding to the formation of solid electrolyte interface (SEI). No obvious cathodic peak is observed after the peak at 1.2 V with an exception of another cathodic peak at *ca.* 0.01 V. This indicates the gradual phase transition during the lithiation process, in lieu of obvious two-phase transition. However, an obvious two-phase transition is occurred during the second cathodic scan, as a distinct peak observed at 0.68 V. These results agree well with the galvanostatic charge-discharge profiles shown in Fig. 3a. During the anodic scan, an obvious peak at 1.0 V can be assigned to the delithiation process. In contrast, anodic peak of TiP_2-C is located at a higher potential of 1.2 V, as indicated in Fig. 3d, which demonstrates the higher polarization of the electrode. This result indicates the multi-phase structure of TiP_2-TiP-P-C electrode with abundant phase interface can enhance the electronic and ionic conductivities, thus reducing the resistance during the charging process and simultaneously accelerating the extraction of Li^+. In the subsequent scans, the well-overlapping of CV curves suggests that TiP_2-TiP-P-C electrode can exhibit high reversibility, good structural integrity, and enhanced cycle stability.

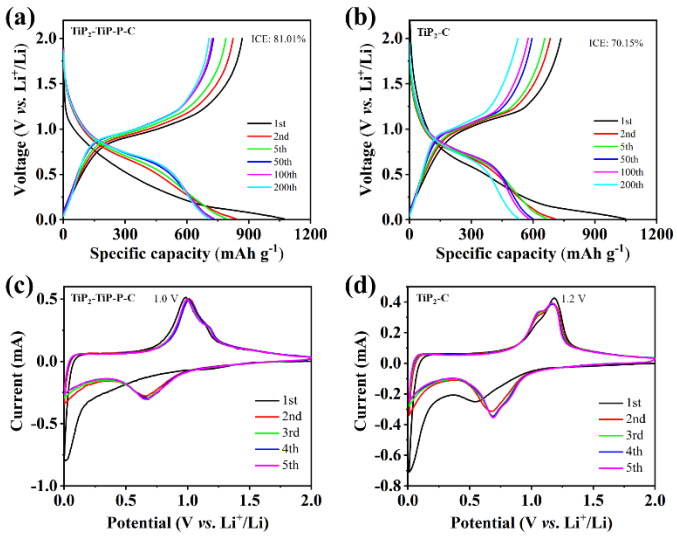

Fig. 3 Galvanostatic discharge/charge curves of (a) TiP_2-TiP-P-C, and (b) TiP_2-C, both at 500 mA g^{-1}. Cyclic voltammetry curves of (c) TiP_2-TiP-P-C, and (d) TiP_2-C, both at 0.1 mV s^{-1}.

Cyclic performance of TiP_2-TiP-P-C and TiP_2-C electrodes were evaluated and compared in Fig. 4a-b at two different current densities of 500 and 2000 mA g^{-1} in a potential window of 0.01-2.0 V. Fig. 4a shows the cyclic performance and coulombic efficiencies upon cycling at a current density of 500 mA g^{-1}. At the relatively low current density of 500 mA g^{-1}, both electrodes exhibit almost similar capacity retention but with differences in terms of capacity and coulombic efficiency. Both TiP_2-TiP-P-C and TiP_2-C exhibit capacity fading within the initial several cycles due to the poor electrical conductivity and volume expansion. After *ca.* 10 cycles, the cyclic performance of both electrodes become stable. TiP_2-TiP-P-C electrode demonstrates the highest reversible specific capacity of 707.1 mAh g^{-1} after 200 cycles, which corresponds to a capacity retention of 81.5%. Furthermore, TiP_2-TiP-P-C electrode has a higher and a generally more stable coulombic efficiency as compared to TiP_2-C, as show in Fig. 4a. It indicates that the multi-phase TiP_2-TiP-P-C electrode can enhance the reversibility of lithiation/delithiation. On the other hand, TiP_2-C electrode has a lower coulombic efficiency which signifies irreversible delithiation and unstable interface reaction result in the continuous decomposition of electrolyte. In addition, Fig. 4b gives the cyclic performance of these two

electrodes, which were cycled at 200 mA g^{-1} for the first three cycles and then subjected to a higher current density of 2000 mA g^{-1}, showing the significant differences between the two electrodes. Comparing with the relatively low current density in Fig. 4a, the obviously higher current density in Fig. 4b would speed up the Li^+ insertion/extraction, which inevitably leads to the rapid decay of structure and thus the capacity attenuation. Consequently, TiP_2-C electrode present a severe decay in specific capacity from 200 cycles. However, TiP_2-TiP-P-C electrode is able to demonstrate excellent cyclic stability with a capacity retention of *ca.* 89.1 % (based on the 4^{th} cycle) after 500 cycles, which is apparently higher than that of *ca.* 39.4 % for TiP_2-C electrode. In order to investigate the role of TiP and amorphous phosphorus, TiP_2-TiP-C and TiP_2-P-C were synthesized and their electrochemical performances are recorded, as shown in Fig. S4 and S5. It shows that TiP_2-TiP-C possesses higher capacity retention and coulombic efficiency than that of TiP_2-C, strongly suggesting the critical role of TiP in effectively stabilizing the structure of TiP_2-TiP-C. More interestingly, the in-situ formed TiP can generate more TiP_2-TiP heterojunction interfaces in TiP_2-TiP-P-C electrode, which can further relive the stress of TiP_2 during the charge/discharge cycling. On the other hand, we find that TiP_2-P-C electrode with phosphorus exhibits a higher electrochemical capacity as compared to TiP_2-C, as shown in Fig. S5c and Fig. S5d, but with similar cyclic stability and coulombic efficiency, suggesting that phosphorus is necessary for the enhancement of capacity. Therefore, the collective results in this study indicate that phosphorus in TiP_2-TiP-P-C can enhance the electrochemical capacity, while TiP acts as effective buffer to improve the cycling stability.

Fig. 4c shows the rate performance of the TiP_2-TiP-P-C and TiP_2 -C electrodes at various current densities between 0.2 to 10 A g^{-1}. According to Fig. 4c, TiP_2-TiP-P-C electrode is able to demonstrate average discharge capacities of 836.3, 733.7, 689.2, 649, 628.4, 597.8, 574.6, and 525.9 mAh g^{-1} at current densities of 0.2, 0.5, 1.0, 2.0, 3.0, 5.0, 7.0, and 10.0 A g^{-1},

respectively. The recorded capacities for TiP_2-TiP-P-C are much higher than these for TiP_2-C electrode (i.e., 743.4, 618, 583.9, 557.1, 542.8, 524.1, 508, and 470.6 mAh g^{-1}). More impressively, Fig. 4c shows that a high specific charge capacity of 722.5 mAh g^{-1} can be recovered for TiP_2-TiP-P-C when the current density returns to 0.5 A g^{-1}, which can be stably existed for additional 70 cycles without any significant capacity degradation. In contrast, TiP_2-C shows an obvious capacity deterioration during the same additional 70 cycles (Figure 4c). This result indicates that TiP_2-TiP-P-C possesses excellent rate performance and outstanding recovery capability as compared to TiP_2-C. The excellent electrochemical performance of multi-phase TiP_2-TiP-P-C composite in this study is further confirmed by comparing with other metal phosphides reported in literature, as shown in Fig. 4d.[3-6, 26-31] Fig. 4e shows the long-term high-rate cyclic performance of TiP_2-TiP-P-C electrode at 5 A g^{-1} with 1000 cycles, demonstrating the excellent cyclic performance with 81.4% capacity retention (based on the 4^{th} cycle) and the cyclic coulombic efficiency with almost 100%. Even the mass loading density of active material increases to 2.5 mg cm^{-2}, an excellent cycle performance of 80.7% retention (based on the 4^{th} cycle) after 200 cycles at 2 A g^{-1} can still be obtained in TiP_2-TiP-P-C composite, as shown in Fig. S6.

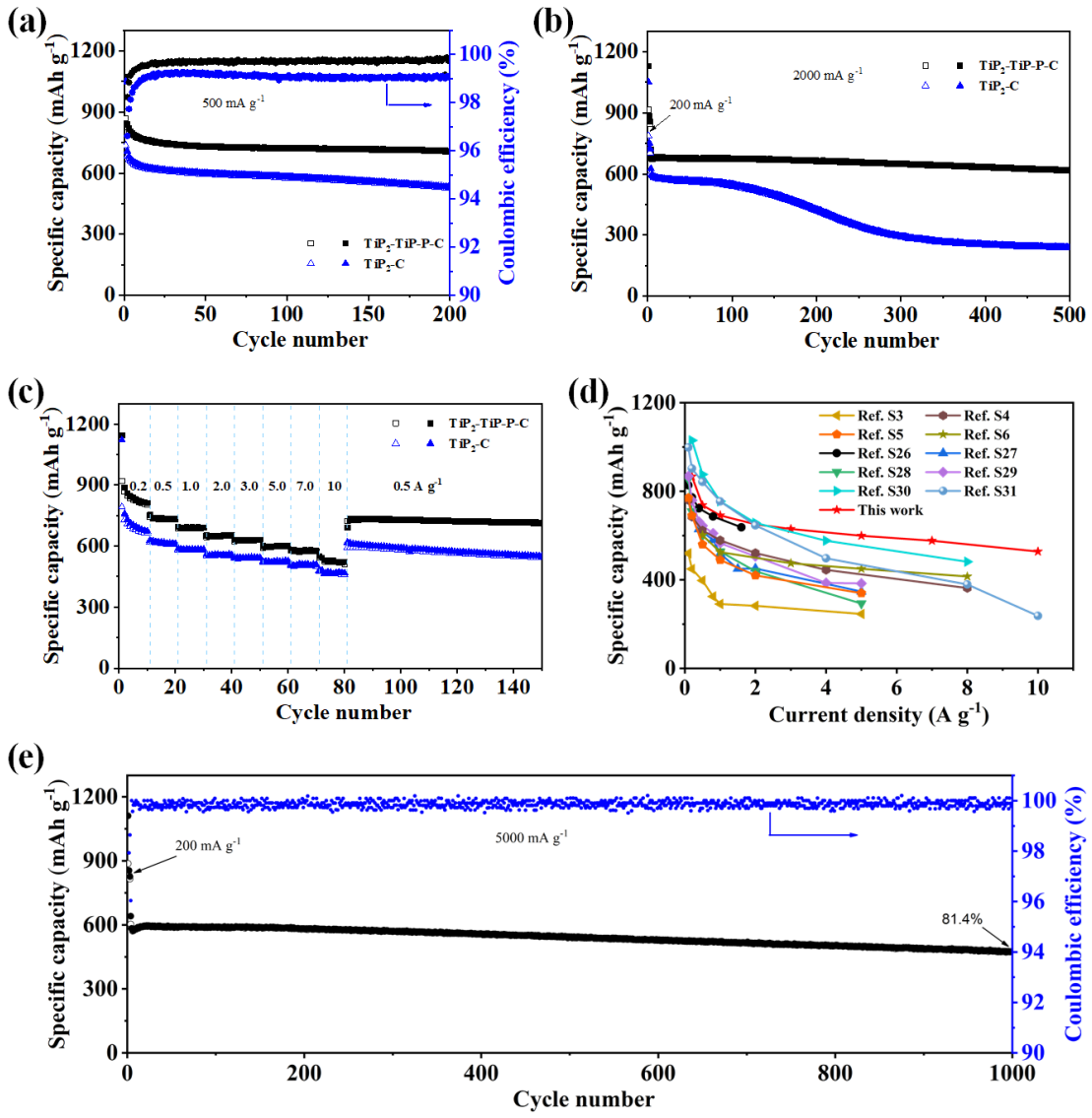

Fig. 4 The electrochemical performance of TiP_2-TiP-P-C and TiP_2-C electrodes. (a) Cyclic performances and coulombic efficiencies conducted at 500 mA g^{-1} for 200 cycles, (b) cyclic performance conducted at 2000 mA g^{-1} for 500 cycles, (c) rate capabilities at various current densities, (d) rate capabilities of recently reported metal phosphides at a range of current densities, and (e) long-term, high current density, cyclic performance of TiP_2-TiP-P-C conducted at 5000 mA g^{-1} for 1000 cycles.

Based on the comparison of phase structure and electrochemical performance between the counterparts, the significant enhancement in cyclic stability at high current density of TiP_2-TiP-P-C might be due to the following factors: (1) The numerous phase interfaces in multi-phase TiP_2-TiP-P-C can effectively restrain the volume change during cycling which is demonstrated by comparing the cycling performance between TiP_2-TiP-P-C and TiP_2-C. (2)

The phosphorus in multi-phase TiP_2-TiP-P-C can increase the electrochemical capacity which is demonstrated by comparing the capacities between TiP_2-TiP-P-C and TiP_2-TiP-C. (3) The carbon matrix in multi-phase TiP_2-TiP-P-C can provide a conductive network so as to enhance the conductivity of the system. To elucidate the mechanisms responsible for the enhanced cyclic stability in TiP_2-TiP-P-C, the SEM morphologies of TiP_2-TiP-P-C and TiP_2-C after 100 cycles at 2 A g^{-1} are respectively given in Fig. 5a and 5b. Due to the slightly volume expansion, it can be observed in Fig. 5a that there are a few fine and narrow cracks on the surface of TiP_2-TiP-P-C electrode. In contrast, higher density of cracks can be clearly observed on the surface of TiP_2-C electrode due to the severely volume expansion, forming the "islands" morphology. The presence of "islands" in TiP_2-C electrode would expose more active electrolyte/electrode interfaces, thus lead to the acceleration in the electrolyte decomposition. This decomposition of electrolyte will then result in the lower coulombic efficiency as shown in Fig. 4a. Fig. 5c-d and Fig. 5e-f present the cross-sectional SEM images of TiP_2-TiP-P-C and TiP_2-C electrodes before and after cycling for 100 cycles at 2 A g^{-1}. The thicknesses of TiP_2-TiP-P-C electrode before cycling is *ca.* 13.1 μm, which is slightly increased by 29.8 % to *ca.* 17.0 μm. In addition the cracks, noticeably, the severely volume expansion in TiP_2-C results in the significant increase in thickness of TiP_2-C electrode with delamination, as shown Fig. 5f, experiencing a 196.0 % increase in thickness, which is larger by 6.5 times as compared to that of TiP_2-TiP-P-C electrode. The significant decrease in volume expansion of TiP_2-TiP-P-C strongly suggests that the multi-phase, *i.e.* TiP_2-TiP, can significantly release the stress and effectively buffer the volume change by formation of TiP, thus demonstrating a remarkable cyclic stability.

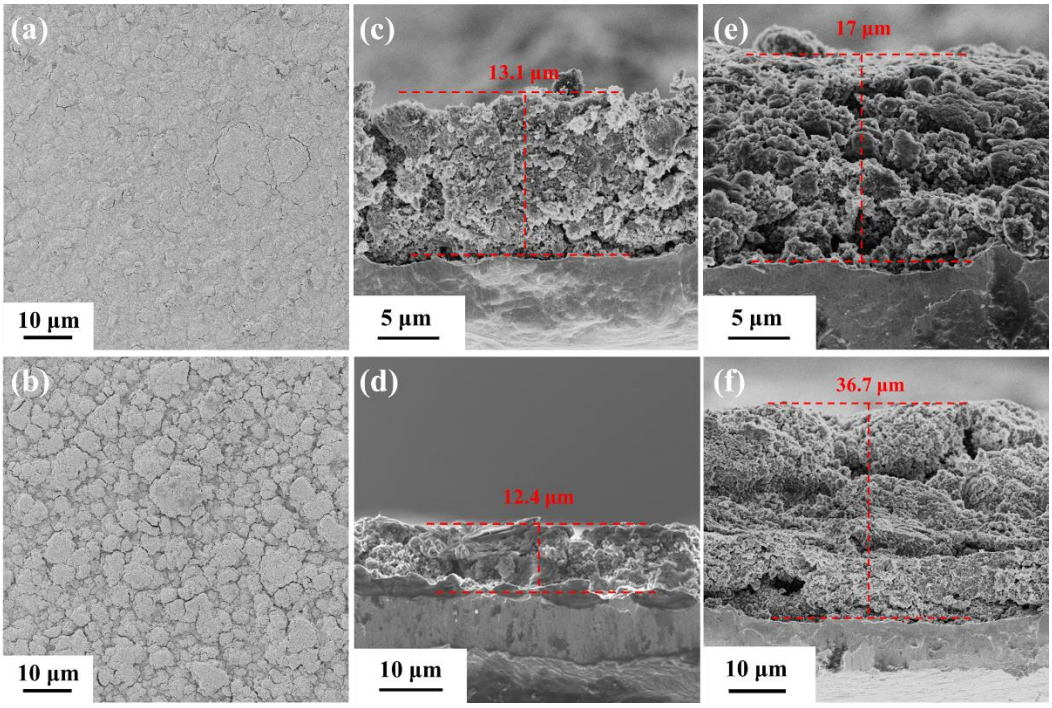

Fig. 5 SEM images of the top-view of (a) TiP_2-TiP-P-C and (b) TiP_2-C after 100 cycles at 2 A g^{-1}. Cross-sectional SEM images of (c) TiP_2-TiP-P-C and (d) TiP_2-C before cycling. Cross-sectional SEM images of (e) TiP_2-TiP-P-C and (f) TiP_2-C after 100 cycles at 2 A g^{-1}.

Multi-phase structure produces a high fraction of interface, which can provide more lithium storage active sites and enhance the interfacial storage efficiency. As a result, excellent electrochemical performance at high rate can be achieved.[19, 32] In order to investigate the electrochemical kinetics mechanisms of TiP_2-TiP-P-C, CV profiles of TiP_2-TiP-P-C and TiP_2-C electrodes are performed at various scan rates between 0.2 to 2.0 mV s^{-1} as shown in Fig. 6a and Fig. S7. According to the relationship between current (i) and scan rate (v) stated by the equation, $i = av^b$, where both a and b are constants, the degree of capacitive effect can be obtained. It has been suggested that the diffusion-controlled process is defined when b approaches 0.5, while surface capacitive-controlled process is dominated when b is close to 1.0.[33, 34] For TiP_2-TiP-P-C electrode, the calculated b-values for anodic and cathodic peaks are 0.82 and 0.88, respectively, which indicate the fast kinetics resulted from the surface capacitive-controlled capacity (Fig. 6b). Total capacitive contribution at a particular scan rate

can be divided into diffusion-controlled ($k_1v^{1/2}$) and capacitive contribution (k_2v) at the corresponding voltage, as described in the Eq. (1):

$$i(V) = k_1v^{1/2} + k_2v \quad (1)$$

Eq. (1) can transformed to Eq. (2) as follow:

$$i(V)/ v^{1/2} = k_1 + k_2 v^{1/2} \quad (2)$$

By calculating k_1 and k_2, the fraction of the capacitive contribution current and diffusion-controlled current can be identified. Accordingly, 83.5% of the overall capacity is determined to be derived from capacitive contribution (blue region) at 1.5 mV s^{-1} as presented in Fig. 6c. Similarly, the contribution ratio of capacitive to diffusion at various scan rates for TiP_2-TiP-P-C and TiP_2-C are respectively shown in Fig. 6d and Fig. S8. It is noted that TiP_2-TiP-P-C demonstrates a higher capacitive contribution as it increases from 71.2% at 0.2 mV s^{-1} to 84.4% at 2.0 mV s^{-1}. The dominating capacitive contribution indicates the abundant interfaces in TiP_2-TiP-P-C.

To further understand the mechanism, galvanostatic intermittent titration technique (GITT) is employed. Fig. S10 shows the 5th GITT cycle measurements and the corresponding responses of these two electrodes. By analyzing the differences between the cut-off voltage and open-circuit voltage measured after 1 h relaxation, the overpotential value (iR) of the electrodes at the 5th cycle can be estimated to describe the resistance during cycling. As shown in Fig. S10c and d, the average overpotential of TiP_2-TiP-P-C during the discharge is 0.0043 V, which is lower than that of TiP_2-C (0.0047 V). This result suggests that TiP_2-TiP-P-C possesses the lowest reaction resistance. The average overpotentials are increased during the charging process in both TiP_2-TiP-P-C and TiP_2-C. However, the increase in average overpotential of TiP_2-C (0.0068 V) is larger than that of TiP_2-TiP-P-C (0.0054 V), which suggests that the multi-phase structure is highly beneficial towards decreasing the Li^+ extract energy barrier,

thus increasing the reaction dynamics. Chemical diffusion coefficients of Li^+ can also be determined from the GITT according to the Eq. (3) and the results are shown in Fig. 6e.[4, 35]

$$D = \frac{4}{\pi\tau}\left(\frac{m_B V_M}{M_B S}\right)^2\left(\frac{\Delta E_s}{\Delta E_\tau}\right)^2 \quad (3)$$

where S (cm^2) represents the effective surface area of active material, τ represents the relaxation time, M_B (g mol^{-1}) is the molar mass of the active material, V_M (cm^3 mol^{-1}) represents the molar volume of the active material, m_B (g) is the mass of the active material, ΔE_τ (V) is the change in voltage during the constant current pulse after the potential drop, and ΔE_s (V) is the change in steady-state voltage. Figure 6e shows that TiP_2-TiP-P-C has a higher Li^+ diffusion coefficient as compared to TiP_2-C, especially obvious higher at the 60% normalized capacity in the charging process. This result indicates that TiP_2-TiP-P-C has a lower Li^+ diffusion energy barrier as compared to TiP_2-C, and therefore result in an excellent diffusion dynamics and rate performance as observed in this study.

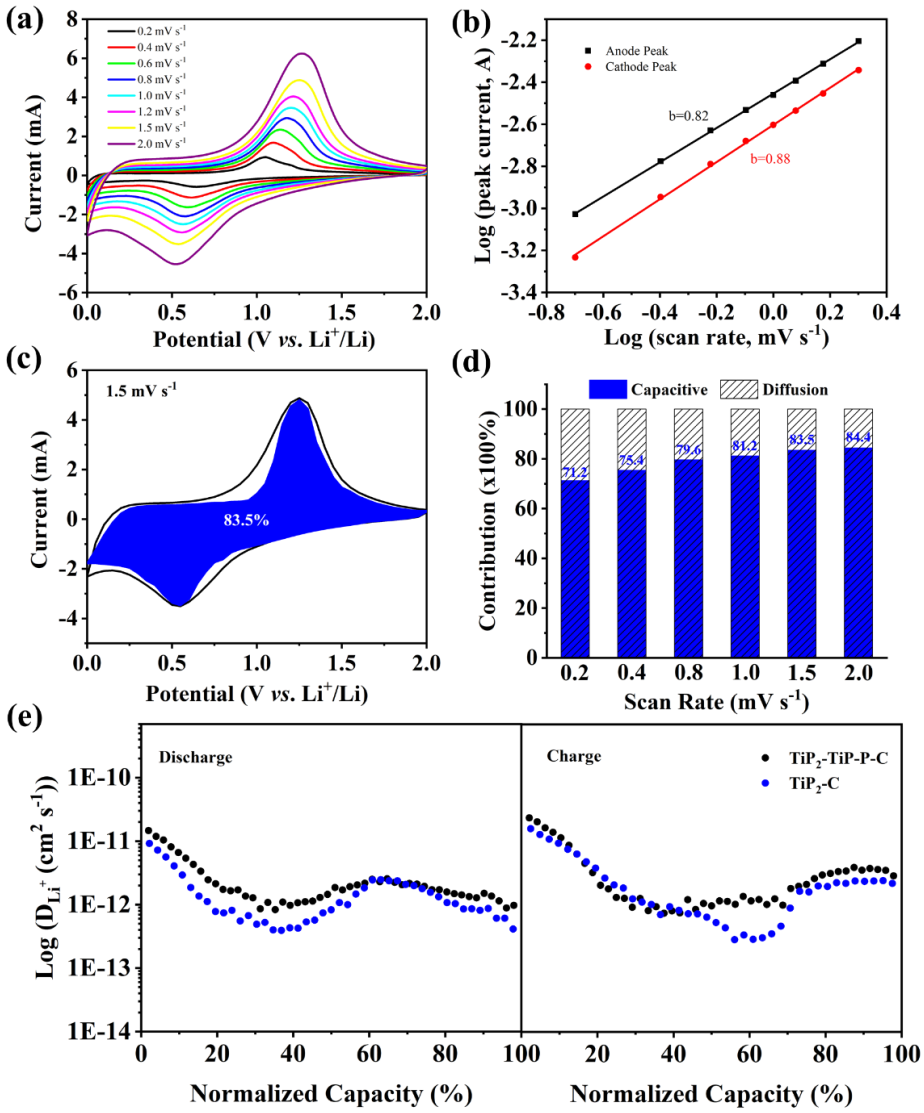

Fig. 6 Kinetic analysis of TiP_2-TiP-P-C for lithium storage. a) CV profiles at various scan rates, b) graph depicting peak current against scan rate, c) ratio of capacitive (blue region) contribution at scan rate of 1.5 mV s^{-1}, d) ratio of capacitive contribution and diffusion-controlled at different scan rates, c) Li^+ diffusion coefficients against normalized capacity.

To further investigate the phase strcuture evolution after de/lithiation, ex-situ XRD was conducted for TiP_2-TiP-P-C at different states of charge as shown in Fig. 7a. After a full discharge process, the characteristic peaks of TiP_2 disappear, while a new weak peak that can be indexed to Li_xTiP_4 ($8.8 < x < 10.2$ as calculation in Fig. S11) phase (isostructural with Li_9TiP_4) appears.[11] No observable Li_3P characteristic peaks are identified in the XRD parttern, which suggests the formation of an amorphous Li_3P phase during lithiation process.

After the full delithiation process, diffraction peak of Li_xTiP_4 phase disappears, indicating that the Li^+ extraction induces the loss of the long-range order of the cubic Li_xTiP_4 phase, which is consistent with the previously reported results.[10, 11]

Based on the collective results, an illustration of the electrochemical reaction processes can be concluded as shown in Fig. 7b. The TiP_2-C composite with less interface has little interfacial storage sites and slow Li^+ diffusion. Interstingly, the TiP_2-TiP-P-C with abundant TiP_2-TiP intrerfaces can simutaneously provide more lithium storage active sites and facilitate the fast Li^+ diffusion. Furthermore, the abundant grain boundaries and electrochemical inactive TiP can effectively restrain the volume change during cycling as shown in Fig. 5c and e.

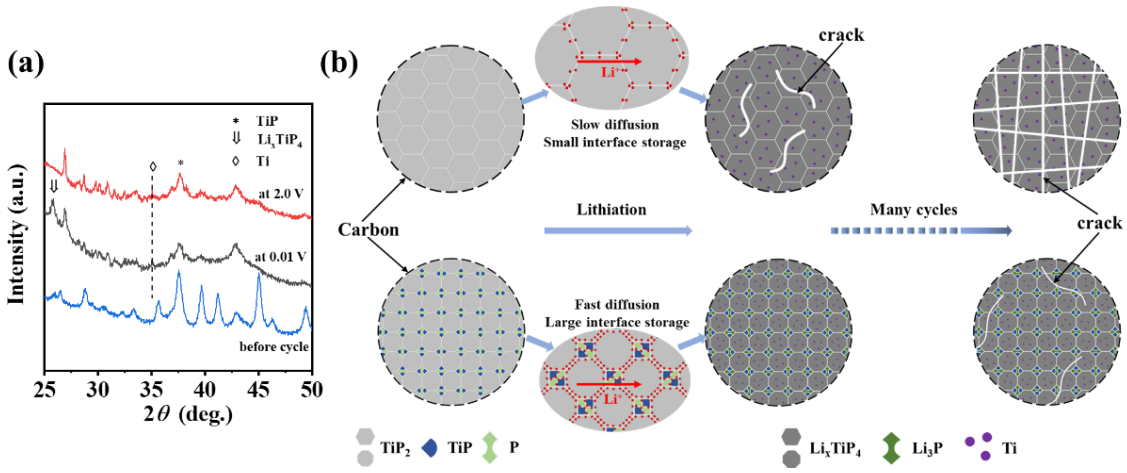

Fig. 7 a) XRD patterns of TiP_2-TiP-P-C before and after cycling at different state of charge, b) illustration of the lithiation storage process of TiP_2-C and multi-phase structured TiP_2-TiP-P-C.

To meet the practical requirement of TiP_2-TiP-P-C, full LIB cell, *i.e.* LFP||TiP_2-TiP-P-C was assembled with $LiFePO_4$ (LFP) as cathode. The galvanostatic charge/discharge profile of LFP||TiP_2-TiP-P-C at 0.5 A g^{-1} in a voltage window of 1.0 to 3.5 V is presented in Fig. 8a. An initial specific charge/discharge capacity of 1031.8 and 745.4 mAh g^{-1} (based on the mass of active material in the anode) with an initial coulombic efficiency (ICE) of 72.24% is obtained. The large initial loss of irreversible lithium might be due to the relative low ICE of TiP_2-TiP-P-C electrode and the formation of SEI on the anode and cathode surfaces. The first five CV

profiles of LFP||TiP_2-TiP-P-C conducted at scan rate of 0.2 mV s^{-1} are presented in Fig. 8b. During the initial charging process, there is no obvious peak except one peak locates around *ca.* 3.5 V. In the subsequent CV cycles, two peaks appear whereby the peak at 2.89 V is attributed to the Li^+ extraction of LFP and the reaction with TiP_2-TiP-P, while the other peak at 3.35 V corresponds to the Li^+ extraction of LFP and the reaction with carbon. In the cathodic process, the main peak located at 2.3 V can be ascribed to the delithiation of TiP_2-TiP-P and lithiation of LFP. Fig. 8c shows the cyclic performance and coulombic efficiency upon cycling at 0.5 A g^{-1} for 70 cycles. It can be observed that the reversible discharge capacity of LFP||TiP_2-TiP-P-C can still be maintained at 637.9 mAh g^{-1} with a capacity retention of 85.6% after 70 cycles. Starting from the fourth cycles, the cyclic coulombic efficiency of LFP||TiP_2-TiP-P-C is *ca.* 96.5%. In addition to the encouraging cyclic performance at low current density, LFP||TiP_2-TiP-P-C is able to show excellent rate performance as indicated in Fig. 8d. The average discharge capacities of 627, 569.5, 523.8, and 487.5 mAh g^{-1} can be achieved at current densities of 3.0, 5.0, 7.0, and 10.0 A g^{-1}, respectively. Notably, a specific capacity as high as 667.4 mAh g^{-1} can be recovered when the current density is switched back to 0.5 A g^{-1} after 40 cycles, indicating the excellent rate capability and outstanding recovery capability. More impressively, Fig. 8e shows that LFP||TiP_2-TiP-P-C is also able to demonstrate excellent cyclic stability of 79.9% at high current density of 5.0 A g^{-1} for 500 cycles (*ca.* 431.7 mAh g^{-1} at the 500^{th} cycle). This excellent cycling performance, especially at high current density, strongly suggests the great potential of utilizing TiP_2-TiP-P-C as a practical LIB anode.

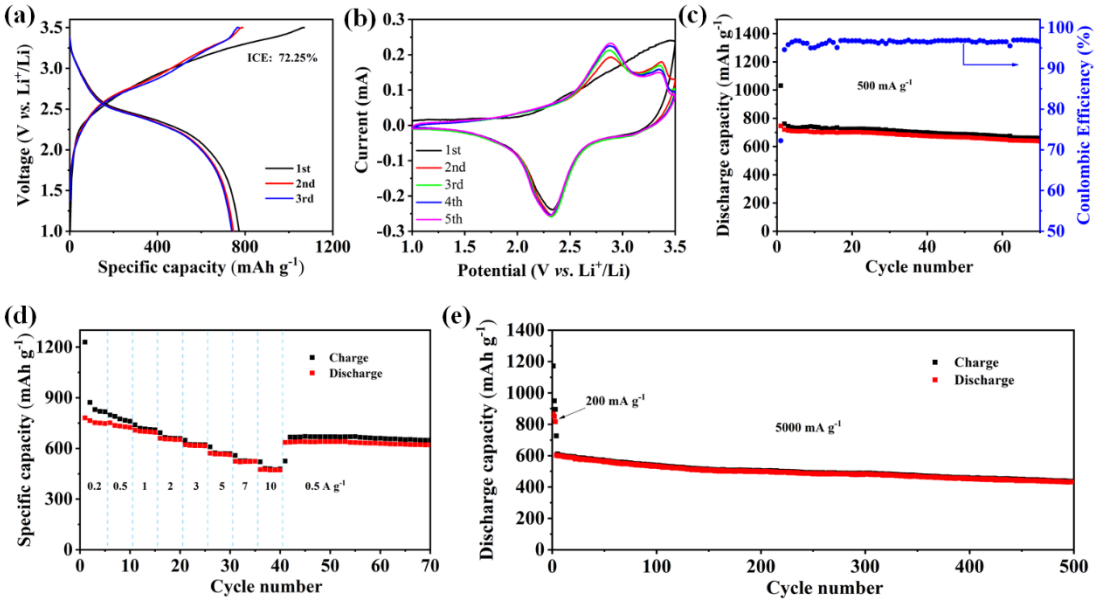

Fig. 8 Electrochemical performance of LFP||TiP_2-TiP-P-C full cell. (a) Galvanostatic charge/discharge profiles between a voltage window of 1.0-3.5 V at 0.5 A g^{-1}, (b) CV curves conducted at 0.2 mV s^{-1}, (c) cyclic performance at 500 mA g^{-1}, (d) rate performance, and (e) long-term, high current density cyclic performance conducted at 5.0 A g^{-1}.

4. Conclusion

This work presents the novel design of multi-phase TiP_2-TiP-P-C as high-performance LIB anode via the decomposition of TiP_2 during ball milling process. The rationale for TiP_2 decomposition is of two folds: (1) one decomposition-formed electrochemically inactive TiP can effectively relieve the stress caused by the formation of Li_xTiP_4 and LiP_3, and (2) another decomposition-formed significant smaller phosphorus can reduce its volume change during lithiation and contribute towards the overall capacity. Accordingly, the multi-phase TiP_2-TiP-P-C is able to demonstrate enhanced cyclic stability due to the cooperative effects of nano-spatial confinement and nano-sizing. The enhanced interfaces in multi-phase TiP_2-TiP-P-C composite can result in more lithium storage active sites and facilitate the Li^+ interfacial storage efficiency, thus demonstrating the excellent electrochemical rate performance. Furthermore, the carbon matrix in multi-phase TiP_2-TiP-P-C can act as a conductive network to enhance the conductivity of the system and a buffer for the drastic volume expansion. As a result, multi-phase TiP_2-TiP-P-C anode displays a high reversible capacity of 868 mAh g^{-1} at 0.5 A g^{-1}, and

a superior rate performance with a high capacity of 525.9 mAh g^{-1} at 10.0 A g^{-1}. More impressively, an ultra-durable cyclic life of 81.4% capacity retention after 1000 cycles at 5 A g^{-1} is also recorded. When TiP_2-TiP-P-C composite is paired with LFP cathode, the LFP||TiP_2-TiP-P-C full cell is able to exhibit excellent capacity and remarkable cycle performance, which indicates its suitability for commercial application. Thus, this work shows that the partial decomposition of TiP_2 to form TiP and P could be a vital strategy towards harmonizing the capacity and cyclic stability in the development of metal phosphide for the further high-performing LIBs.

Acknowledgements

This work was financially supported by the Foundation for Innovative Research Groups of the National Natural Science Foundation of China (No. NSFC51621001), National Natural Science Foundation of China Projects (Nos. 51771075 and 51971187) and by the Project Supported by Natural Science Foundation of Guangdong Province of China (2016A030312011).

References

[1] J. Choi, W.S. Kim, K.H. Kim, S.H. Hong, J. Mater. Chem. A, 6 (2018) 17437-17443.

[2] M. Zhang, R.Z. Hu, J.W. Liu, L.Z. Ouyang, J. Liu, L.C. Yang, F. Fang, M. Zhu, J. Alloys Compd., 762 (2018) 246-253.

[3] C. Wu, P. Kopold, P.A. van Aken, J. Maier, Y. Yu, Adv. Mater., 29 (2017).

[4] X.J. Xu, J.R. Feng, J. Liu, F. Lv, R.Z. Hu, F. Fang, L.C. Yang, L.Z. Ouyang, M. Zhu, Electrochim. Acta, 312 (2019) 224-233.

[5] Z. Liu, S. Yang, B. Sun, X. Chang, J. Zheng, X. Li, Angew. Chem. Int. Ed., 57 (2018) 10187-10191.

[6] C.R. Ma, C.J. Deng, X.Z. Liao, Y.S. He, Z.F. Ma, H. Xiong, ACS Appl. Energy Mater., 1 (2018) 7140-7145.

[7] S.O. Kim, A. Manthiram, Chem. Commun., 52 (2016) 4337-4340.

[8] M.P. Bichat, F. Gillot, L. Monconduit, F. Favier, M. Morcrette, F. Lemoigno, M.L. Doublet, Chem. Mater., 16 (2004) 1002-1013.

[9] F. Gillot, L. Monoconduit, M. Morcrette, M.L. Doublet, L. Dupont, J.M. Tarascon, Chem. Mater., 17 (2005) 3627-3635.

[10] F. Gillot, M.P. Bichat, F. Favier, M. Morcrette, M.L. Doublet, L. Monconduit, Electrochim. Acta, 49 (2004) 2325-2332.

[11] S.-g. Woo, J.-H. Jung, H. Kim, M.G. Kim, C.K. Lee, H.-J. Sohn, B.W. Cho, J. Electrochem. Soc., 153 (2006) A1979-A1983.

[12] X. Wang, H.M. Kim, Y. Xiao, Y.K. Sun, J. Mater. Chem. A, 4 (2016) 14915-14931.

[13] X. He, R. Wang, M.C. Stan, E. Paillard, J. Wang, H. Frielinghaus, J. Li, Adv. Mater. Interfaces, 4 (2017) 1601047.

[14] S.-O. Kim, A. Manthiram, Chem. Mater., 28 (2016) 5935-5942.

[15] P.-O. Snell, Acta Chem. Scand., 21 (1967) 1773-1776.

[16] W.-C. Chang, K.-W. Tseng, H.-Y. Tuan, Nano Lett., 17 (2017) 1240-1247.

[17] Y.M. Sun, L. Wang, Y.B. Li, Y.Z. Li, H.R. Lee, A. Pei, X.M. He, Y. Cui, Joule, 3 (2019) 1080-1093.

[18] R. Hu, Y. Ouyang, T. Liang, H. Wang, J. Liu, J. Chen, C. Yang, L. Yang, M. Zhu, Adv. Mater., 29 (2017).

[19] D. Cheng, L. Yang, J. Liu, R. Hu, J. Liu, K. Pei, M. Zhu, R. Che, J. Mater. Chem. A, 7 (2019) 15320-15332.

[20] J. Sun, G. Zheng, H.W. Lee, N. Liu, H. Wang, H. Yao, W. Yang, Y. Cui, Nano Lett., 14 (2014) 4573-4580.

[21] Y.M. Sun, X.L. Hu, W. Luo, F.F. Xia, Y.H. Huang, Adv. Funct. Mater., 23 (2013) 2436-2444.
[22] W.-J. Li, S.-L. Chou, J.-Z. Wang, H.-K. Liu, S.-X. Dou, J. Mater. Chem. A, 4 (2016) 505-511.
[23] C.E. Myers, H.F. Franzen, J.W. Anderegg, Inorg. Chem., 24 (1985) 1822-1824.
[24] Y. Wu, F.F. Xing, R. Xu, X.L. Cheng, D.J. Li, X.F. Zhou, Q.B. Zhang, Y. Yu, J. Mater. Chem. A, 7 (2019) 8581-8588.
[25] Q. Huang, S. Tian, D. Zeng, X. Wang, W. Song, Y. Li, W. Xiao, C. Xie, ACS Catal., 3 (2013) 1477-1485.
[26] S.O. Kim, A. Manthiram, ACS Appl. Mater. Interfaces, 9 (2017) 16221-16227.
[27] F. Han, C.Z. Zhang, J.X. Yang, G.Z. Ma, K.J. He, X.K. Li, J. Mater. Chem. A, 4 (2016) 12781-12789.
[28] G.L. Xia, J.W. Su, M.S. Li, P. Jiang, Y. Yang, Q.W. Chen, J. Mater. Chem. A, 5 (2017) 10321-10327.
[29] X. Wang, P. Sun, J. Qin, J. Wang, Y. Xiao, M. Cao, Nanoscale, 8 (2016) 10330-10338.
[30] X. Wang, K. Chen, G. Wang, X. Liu, H. Wang, ACS Nano, 11 (2017) 11602-11616.
[31] M.J. Zhang, J.Y. Yu, T.P. Ying, J.H. Yu, Y.P. Sun, X.G. Liu, J. Alloys Compd., 777 (2019) 860-865.
[32] B. Long, M.S. Balogun, L. Luo, W.T. Qiu, Y. Luo, S.Q. Song, Y.X. Tong, Adv. Energy Mater., 8 (2018).
[33] V. Augustyn, J. Come, M.A. Lowe, J.W. Kim, P.L. Taberna, S.H. Tolbert, H.D. Abruna, P. Simon, B. Dunn, Nat. Mater., 12 (2013) 518-522.
[34] D. Chao, P. Liang, Z. Chen, L. Bai, H. Shen, X. Liu, X. Xia, Y. Zhao, S.V. Savilov, J. Lin, Z.X. Shen, ACS Nano, 10 (2016) 10211-10219.
[35] W.W. Zeng, L. Wang, X. Peng, T.F. Liu, Y.Y. Jiang, F. Qin, L. Hu, P.K. Chu, K.F. Huo, Y.H. Zhou, Adv. Energy Mater., 8 (2018) 1702314.

Boosted lithium storage cycling stability of TiP_2 by *in-situ* partial self-decomposition and nano-spatial confinement

Fengchen Zhou[a], Xu-Sheng Yang[c,d*], Jiangwen Liu[a], Jun Liu[a], Renzong Hu[a], Liuzhang Ouyang[a,b**], Min Zhu[a]

[a] School of Materials Science and Engineering, Guangdong Provincial Key Laboratory of Advanced Energy Storage Materials, South China University of Technology, Guangzhou, 510641, China. Email: meouyang@scut.edu.cn

[b] China-Australia Joint Laboratory for Energy & Environmental Materials, Key Laboratory of Fuel Cell Technology of Guangdong Province, Guangzhou, 510641, China

[c] Advanced Manufacturing Technology Research Centre, Department of Industrial and Systems Engineering, The Hong Kong Polytechnic University, Hung Hom, Kowloon, Hong Kong, China. Email: xsyang@polyu.edu.hk

[d] Hong Kong Polytechnic University Shenzhen Research Institute, Shenzhen 518057, China

[*]Corresponding authors.
[a**] E-mail: meouyang@scut.edu.cn, (L. Ouyang)
[c*] E-mail: xsyang@polyu.edu.hk, (X. Yang)

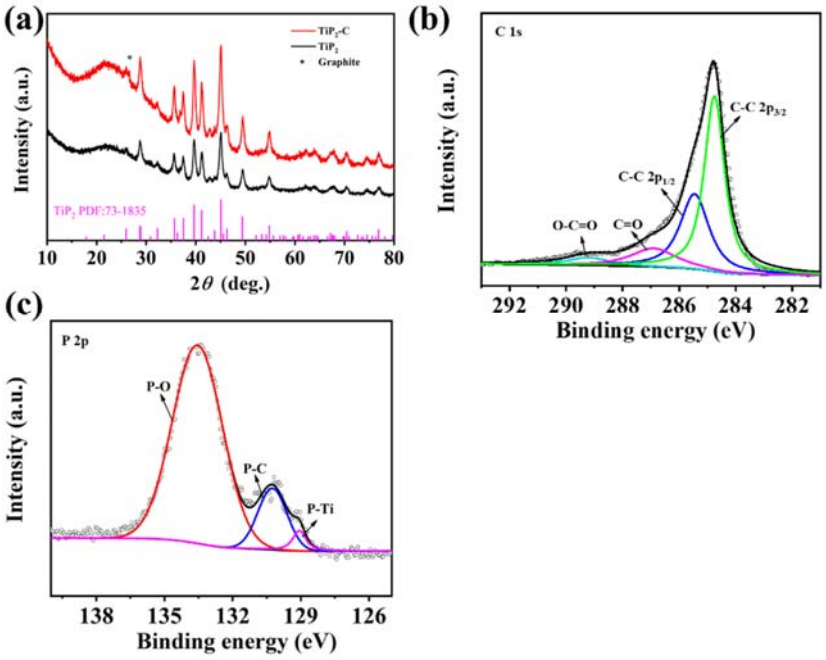

Fig. S1 (a) the XRD patterns of TiP_2 and TiP_2-C composites. High-resolution XPS spectra of (b) C 1s, (c) P 2p of TiP_2-C.

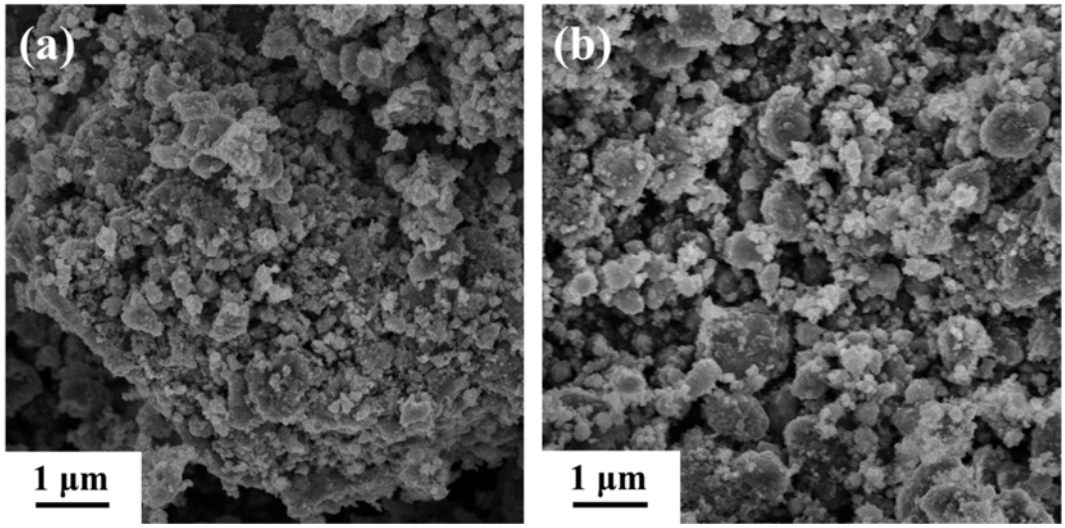

Fig. S2 SEM images of (a) TiP_2, (b) TiP_2-C nanocomposite.

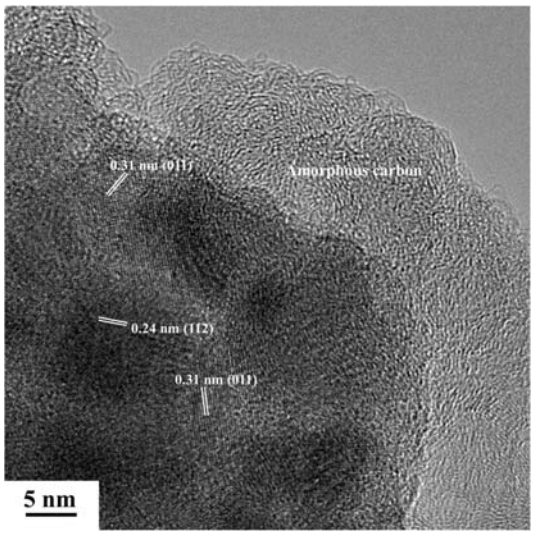

Fig. S3 HRTEM images of TiP_2-C nanocomposite.

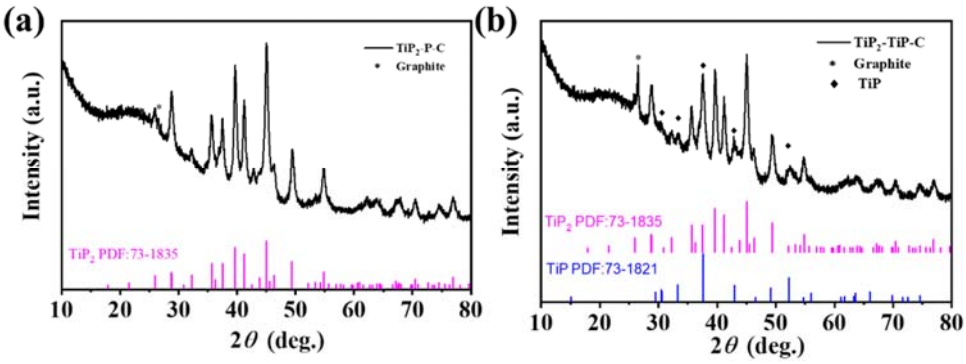

Fig. S4 The XRD patterns of (a) TiP_2-P-C and (b) TiP_2-TiP-C composites.

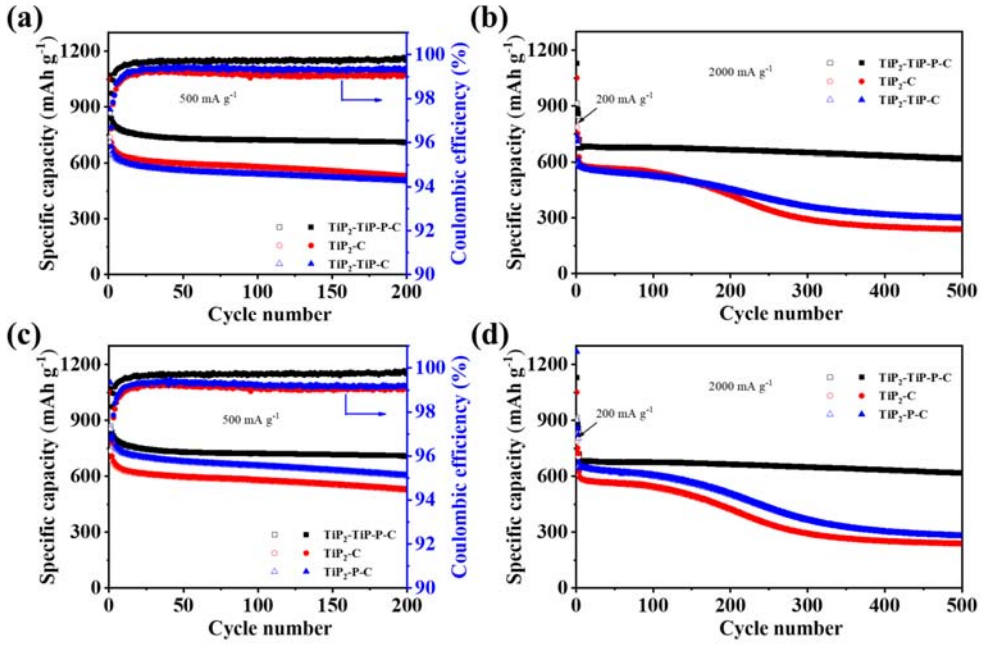

Fig. S5 Electrochemical performance of TiP_2-TiP-P-C, TiP_2-C, TiP_2-TiP-C and TiP_2-P-C electrodes. (a, c) the cycle performances and coulombic efficiency at 500 mA g^{-1}, (b, d) the cycle performances at 2000 mA g^{-1}.

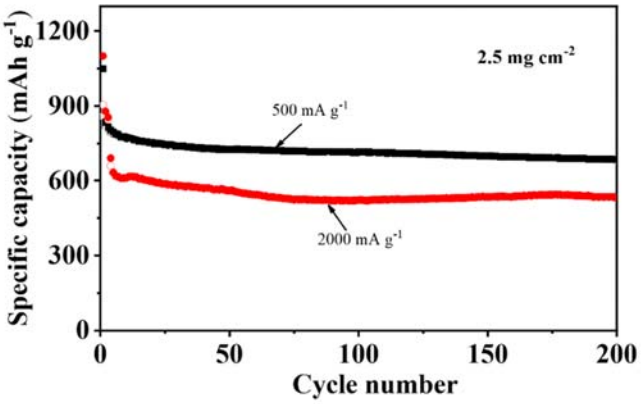

Fig. S6 Cycle performances of TiP_2-TiP-P-C at different current densities with an active material load of 2.5 mg cm^{-2}.

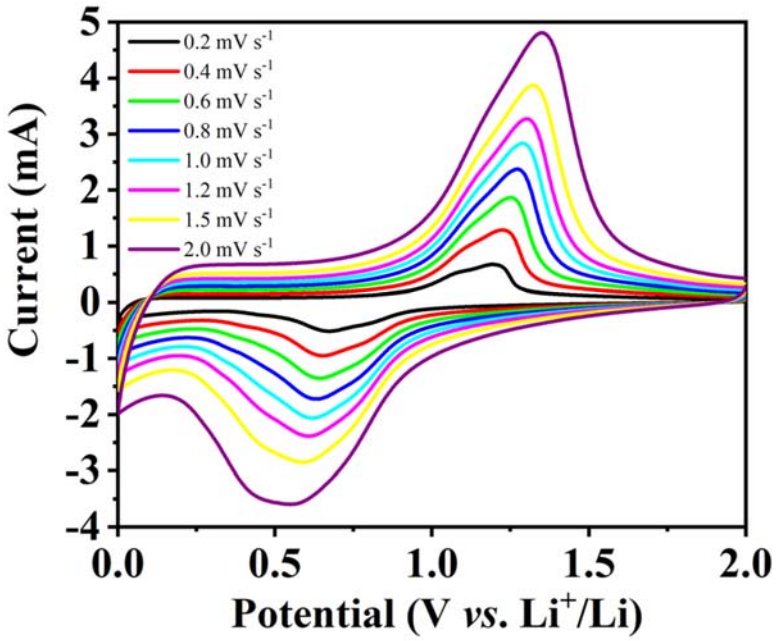

Fig. S7 CV curves of TiP_2-C at various scan rates, from 0.2 to 2.0 mV s^{-1}.

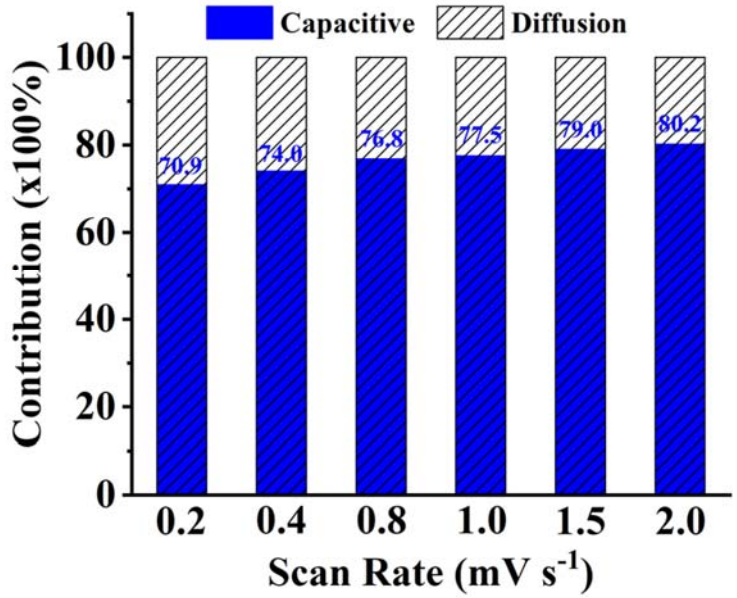

Fig. S8 Pseudocapacitive contribution at different scan rates of TiP_2-C.

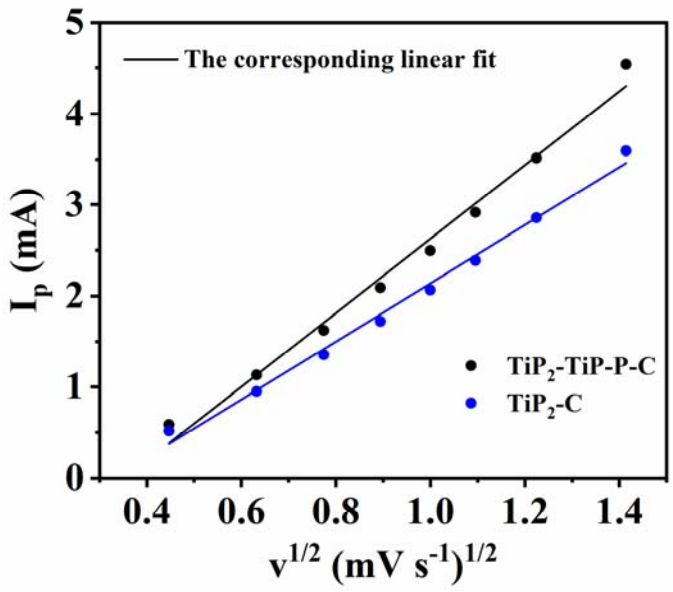

Fig. S9 Corresponding relationship between peak currents and sweep rates of the TiP_2-TiP-P-C and TiP_2-C.

The anodic peak currents Ip at different scan rates are adopted to calculate the Li^+ diffusion coefficients (D) of these electrodes according to the following Randles Sevcik equation: $Ip = 2.69\times10^5 ACD^{1/2}n^{3/2}\upsilon^{1/2}$, where A stands for the anode area (cm^2), C is for the shuttle concentration (mol cm^{-3}), n is for the involved electron numbers in the redox action, and υ is for the scan rate (V s^{-1}). With this data, a fitting straight-line can be obtained with $\upsilon^{1/2}$ as the x-axis and Ip as the y-axis. Therefore, the line slope and Li^+ diffusion coefficient can be calculated. As shown in Fig. S9, the TiP_2-TiP-P-C has a higher slope, suggesting the larger Li^+ diffusion coefficient. The result is matched well with the result calculated by GITT.

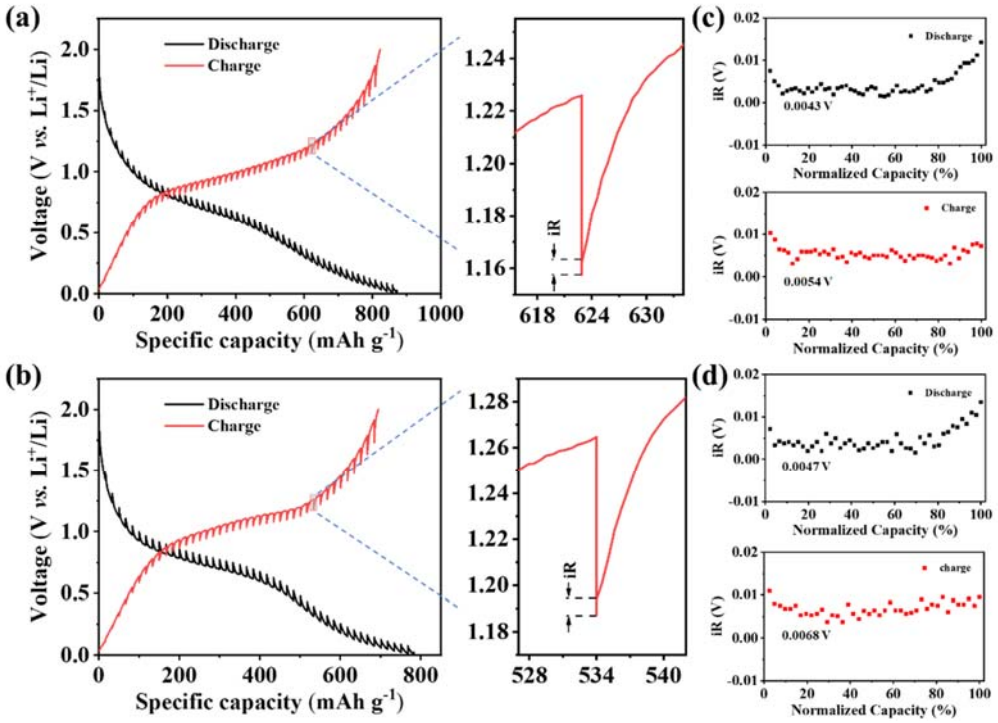

Fig. S10 Potential response curves of (a) TiP_2-TiP-P-C and (b) TiP_2-C during the 5th cycle GITT measurements with the inset of the magnified area illustrating the overpotential (iR). (c, d) Overpotential values estimated from the GITT results for 5th cycle.

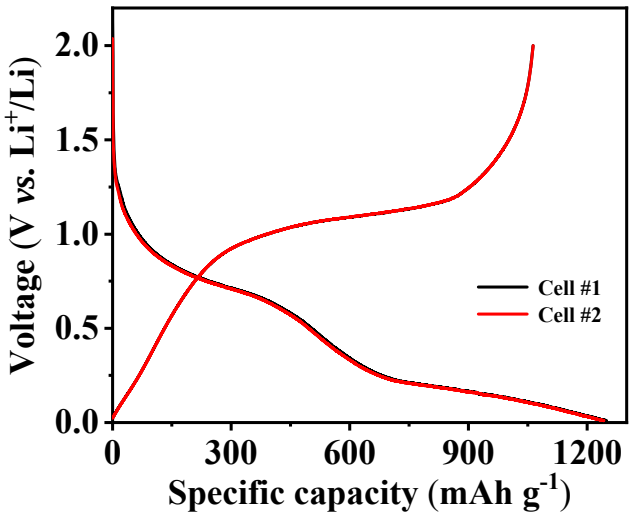

Fig. S11 Initial voltage profiles of TiP_2 electrode with different cells at a current density of 50 mA g^{-1}.

Base on the reaction during lithiation:

$2TiP_2 + xLi + xe^- \rightarrow Li_xTiP_4 + Ti$

And the theoretical capacity calculation formula:

$Q_{theoretical} = (nF) / (3.6*M_w)$

n is the number of charge carrier, F is the Faraday constant and M_w is the molecular weight of the active material used in the electrode.

So according to the initial charge/discharge capacity of TiP_2, the x value between 8.8 to 10.2.